Thin-Walled Carbon Microtubes as High-Capacity and High-Rate Anodes in Lithium-Ion Batteries

Praveen Meduri, Jeong H. Kim, and Harry B. Russell

Department of Chemical Engineering and Conn Center for Renewable Energy Research, University of Louisville, Louisville, Kentucky 40292

Jacek Jasinski

Conn Center for Renewable Energy Research, University of Louisville, Louisville, Kentucky 40292

Gamini U. Sumanasekera

Department of Physics and Conn Center for Renewable Energy Research, University of Louisville, Louisville, Kentucky 40292

Mahendra K. Sunkara*

Department of Chemical Engineering and Conn Center for Renewable Energy Research, University of Louisville, Louisville, Kentucky 40292

In this article, we present a large-area synthesis of carbon microtubes (CMTs) with internal diameters of $\sim$1.5 μm and wall thicknesses on the order of 50 nm and their lithium ion intercalation and deintercalation properties for the first time. The results show that CMTs exhibit a good capacity retention of 443 mAh g^{-1} after 20 cycles, higher than the theoretical capacity of graphite and $\sim$1.5 times higher than the capacity of multi-walled carbon nanotubes at similar conditions. The high capacity retention is attributed mostly to the presence of nanodomains of graphite in the thin walls of the microtubes providing multiple pathways for lithium ion intercalation and the open ends of the CMTs providing additional surface area for intercalation. The CMTs show good rate capability with a capacity retention of 135 mAh g^{-1} at a current density of 1.5 A g^{-1}.

Introduction

Energy storage is gaining tremendous significance, and the need for high-energy density storage systems is constantly on the rise. Rechargeable lithium-ion (Li-ion) batteries have been demonstrated to be the best state-of-the-art energy storage devices.[1,2] In particular, highly graphitized as well as hard carbon materials have been extensively studied and used as anode materials in Li-ion batteries because of their numerous advantages, such as inexpensive synthesis, large-scale availability, low environmental impact, good chemical stability, and low potential with respect to lithium metal. However, highly graphitized materials have a low specific capacity (theoretical capacity of 372 mAh g^{-1} corresponding to LiC$_6$),[3] limited rate capability, and lithium metal plating at low voltages, where most of the specific capacity arises for these materials. Hard carbons[4,5] and disordered carbons,[6] on the other hand, show a higher theoretical capacity than graphite of up to LiC$_2$, due to the turbostatic disorder in the graphene sheets, but have a limited rate capability. To overcome these problems, single-walled and multi-walled carbon nanotubes (SWCNTs and MWCNTs),[7–9] carbon nanofibers (CNFs),[10] and porous carbon materials[11,12] have been studied as possible anode materials for Li-ion batteries. Their nanoscale dimensions provide a higher surface area-to-volume ratio, allowing higher Li ion intercalation, thus

increasing the material specific capacity. Although these materials show high initial capacities in the range of 700−1500 mAh g^{-1},[7,12−15] most of them have ordered wall structures with long pathways, which complicates Li ion intercalation/deintercalation due to longer Li ion diffusion lengths and fewer pathways. Hence, these materials tend to show low to moderate rate capability and moderate capacities with cycling. In addition to the carbon anodes, other inorganic anode materials, including cobalt oxide,[16] tin oxide,[17] modified metal oxide hybrid architectures,[18] and silicon nanowires,[19] have shown good capacity retention, but the rate capability still needs to be addressed. A few reports based on carbon nanofibers,[20,21] milled graphite,[22] porous carbon materials,[23] carbon nanobeads,[24,25] and carbon nanosprings[26] have shown good rate capabilities, but large-area synthesis of these materials is still a challenge.

Carbon microtubes (CMTs) are another morphological form of carbon with micrometer scale internal diameters and thin walls made of nanodomains of graphite. Thin-walled CMTs were originally synthesized using gallium (Ga), and the Ga-filled, straight CMTs were suggested as nanothermometers.[27] Later, thin-walled CMT synthesis with control over the conical angles and microtube diameters was demonstrated.[28,29] Another study showed that these CMTs can be synthesized during thermal decomposition of a Ga precursor.[30] Recently, Sn particles encapsulated in porous multichannel carbon microtubes have shown a capacity retention of $\sim$650 mAh g^{-1} after 140 cycles.[31] In our present study, for the first time, we report the

* To whom correspondence should be addressed. E-mail: mahendra@ louisville.edu. Tel: +1 (502) 852-1558. Fax: +1 (502) 852-6355.

large-area synthesis strategy of CMTs and their electrochemical characteristics. As discussed earlier in our study,[29] the walls of CMTs can be distinctively different from carbon nanotubes in terms of graphene planes and crystallinity. The structural characteristics suggest that CMTs with large internal diameters and nanocrystallinity within thinner walls present short diffusion lengths for Li ions and thus can be potentially interesting as anodes in Li-ion batteries specifically with good rates. There is no prior data or work on the Li intercalation properties of CMTs. In this study, gram quantities of CMTs are synthesized and characterized for Li ion intercalation capacity and performance at different charge−discharge rates.

Experimental Methods

Synthesis of CMTs. CMTs were synthesized on 6 in. silicon wafers in a metal organic chemical vapor deposition reactor at a substrate temperature of 700 °C. The chamber pressure was set to 50 Torr with a carrier gas (nitrogen) flow rate of 10 sccm, and the precursor, trimethyl gallium, was set at 0 °C. A 10 min experiment covered the entirety of the silicon wafer with CMTs, and the mass of the sample obtained for each run was more than 200 mg. CMTs were then scraped off the silicon wafers and dispersed in aqua regia to dissolve off the gallium. Aqua regia was freshly prepared by making a solution of concentrated nitric acid (Fisher Scientific) and concentrated hydrochloric acid (Fisher Scientific) in a volumetric ratio of 1:3. The CMTs were allowed to stand in the acid solution for an hour before removing the settled deposit of the CMTs from the solution. The CMTs were then washed with water and then dried at 200 °C for a couple of hours.

Characterization. The as-synthesized as well as the postlithiated CMT samples were characterized for their structure and morphology using scanning electron microscopy (SEM) (FEI Nova 600) and transmission electron microscopy (TEM) (FEI Tecnai F20 with a Gatan 2002 GIF system). The crystal structure of the samples was studied using X-ray diffraction (XRD) (Bruker D8 Discover, Cu Kα radiation) and Raman spectroscopy (in-Via Renishaw micro-Raman system with a cooled CCD detector) with a HeNe laser (632.8 nm) as an excitation source. The BET surface area was determined by the nitrogen adsorption/desorption data obtained using the Micromeretics TriStar 3000.

Lithium-Ion Battery Measurements. CMTs were mixed with poly(vinylidene fluoride) in a weight ratio of 90:10, respectively, using 1-methyl-2-pyrrolidone as the solvent. The paste was then coated onto a copper foil and hard pressed before drying the electrode in a vacuum oven at a temperature of 110 °C overnight. A three-electrode cell was employed for all the electrochemical measurements with CMTs as the working electrode and the lithium metal as both the auxiliary and the reference electrodes in an electrolyte consisting of 1 M lithium hexaflourophosphate (LiPF$_6$) mixed in a 1:1 volumetric ratio of ethylene carbonate (EC) and diethyl carbonate (DEC). The cell was assembled in an argon-filled glovebox (Vacuum Atmospheres Company) free of moisture and oxygen. All the electrochemical measurements were carried out inside the argon glovebox at room temperature using an eDAQ potentiostat and e-corder.

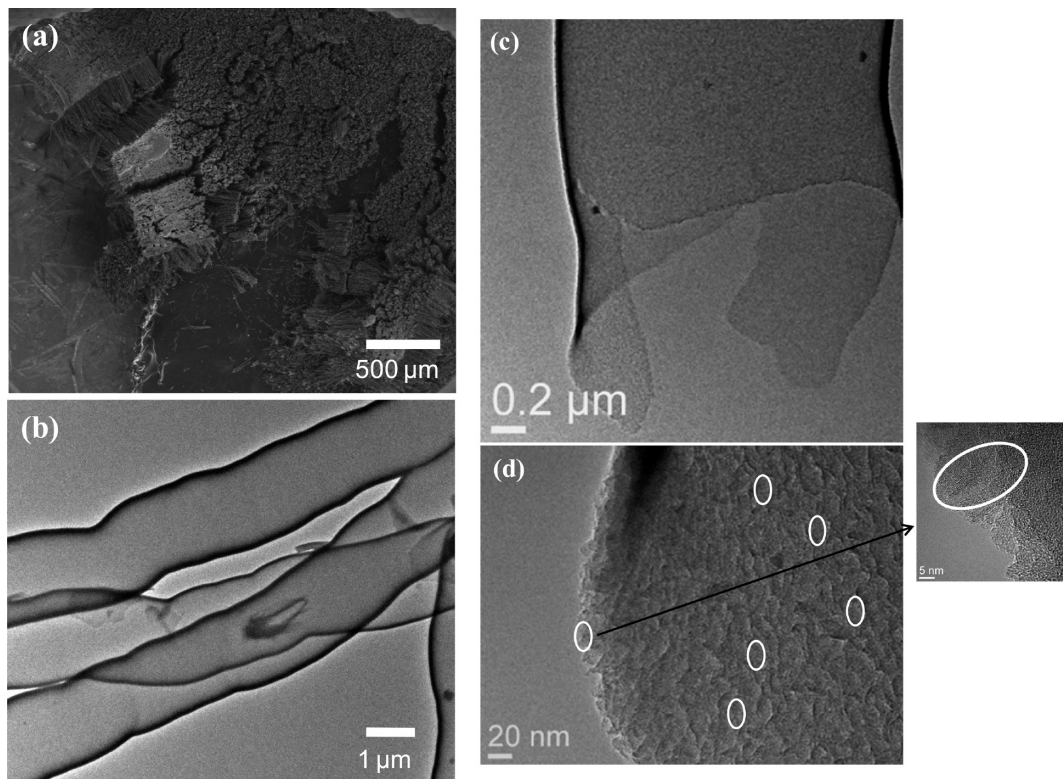The differential capacity curves are calculated using the equation

$$dq/mdV = (I/m)([t(n + 1) - t(n)]/[V(n + 1) - V(n)]) \tag{1}$$

where I is the current, m is the mass of the material, and $V(n + 1)$ and $V(n)$ are the adjacent voltage data points at the adjacent time data $t(n + 1)$ and $t(n)$. The Coulombic efficiency was calculated as the ratio of the charge capacity to the discharge capacity.

Results and Discussion

CMTs are synthesized by the decomposition of trimethyl gallium at 700 °C, giving rise to Ga metal and methyl radical species; the Ga then catalyzes the growth of CMTs. CMTs are synthesized as arrays directly on silicon (Si) substrates. The CMT synthesis procedure and the structure have been described in detail elsewhere.[28−30] Although the present technique of using trimethyl gallium is expensive, this process presents a route of using Ga as a catalyst in the presence of methyl radical species for the inexpensive large-area synthesis of CMTs. The SEM image in Figure 1a shows a large area of the as-synthesized CMTs that are several micrometers in length. The cleaned CMTs shown in the TEM image in Figure 1b indicate that the aqua regia has dissolved off the gallium even on the inside of the CMTs, which are ∼1.5 μm in diameter. An energy-dispersive X-ray (EDX) spectrum of the cleaned samples shows that the microtubes are devoid of gallium (Figure S1 in the Supporting Information). The wall thickness, as determined from the TEM image in Figure 1c, is ∼50 nm. Figure 1d is a high-resolution TEM (HRTEM) image of a single CMT clearly showing the wall structure that is covered with random rotations and translations of nanodomains of graphite crystals. The inset of Figure 1d further shows the structure of a single graphite nanodomain. The interlayer spacing d_{002} of the graphite nanodomains, as calculated from the HRTEM image, is 0.353 Å. It is apparent from the images that CMTs are inherently open-ended, unlike the carbon nanotubes (CNTs), which have closed ends in most cases, providing additional surface area inside the tube interiors. CMTs have a Brunauer−Emmett−Teller (BET) surface area of 78 m^2/g, according to the N$_2$ adsorption isotherm, considerably high for micrometer scale materials. This value is lower than the estimated theoretical capacity of 212 m^2/g for CMTs that are 150 μm long and 1.5 μm in diameter, probably due to the bundling of the CMTs, reducing the specific surface area.

Raman spectroscopy is one of the most widely used techniques to study the carbon atom bonding states. The Raman spectrum of the as-synthesized CMTs in Figure 2a shows two distinct peaks at 1334 and 1591 cm^{-1}, corresponding to the D and G bands in the carbon structures, respectively. The peak at 1591 cm^{-1} corresponds to the graphite E$_{2g}$ mode, although the actual peak is at 1584 cm^{-1}. The peak shift toward the higher wavenumbers has been attributed to the metal incorporation in disordered carbons, which leads to breaking of the sp^2 bonds with the formation of shorter carbon chains.[32] The D band in the spectrum corresponds to the A$_{1g}$ symmetry, which arises from the disordered carbon, in this case, due to the nanocrystalline domains of graphite in the walls and the open ends of CMTs.[33,34] The ratio of the intensity of the D band to the G band indicates the degree of disordered carbon in the material, which, for CMTs, is 1.05. The XRD spectrum of the pure CMTs is shown in Figure 2b. The peak at $2\theta \approx 25.2°$ is characteristic of the (002) graphite plane. The interlayer distance d_{002} of the CMTs is 3.53 Å, which is higher than the d_{002} of graphitic carbon (3.35 Å). The increased interlayer distance is usually the characteristic of graphite and/or carbon nanotubes that are ball-milled for up to 100 h. Moreover, the peak at $2\theta \approx 31.6°$ is the characteristic of ball-milled graphite, which is clearly identified

Thin-Walled CMTs as Anodes in Li-Ion Batteries

J. Phys. Chem. C, Vol. 114, No. 23, 2010 **10623**

Figure 1. Representative image of (a) large areas of bundled CMTs in SEM. (b) Clean CMTs devoid of Ga after treatment in aqua regia. (c) TEM image showing the CMT diameter and wall thickness of ~50 nm. (d) CMT wall domains in a HRTEM. The inset shows the structure of a single graphite nanodomain.
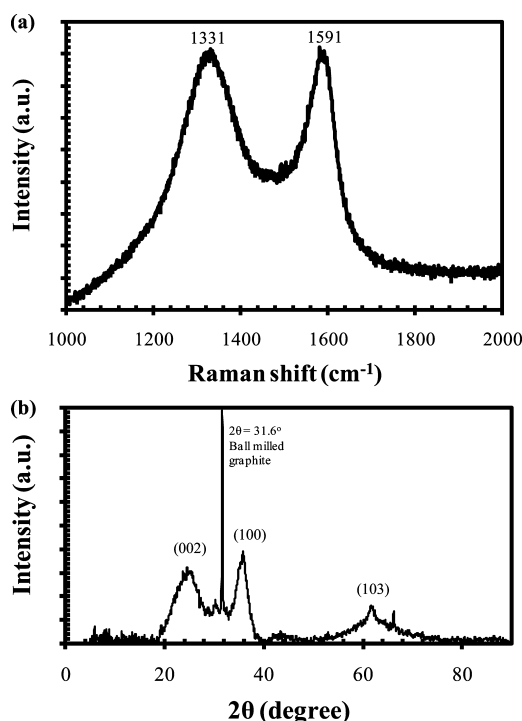

Figure 2. Characterization of cleaned CMTs using (a) Raman spectroscopy for the bonding state of the carbon atoms. (b) XRD spectrum showing the material crystal structure and phase.

in other studies.[35] The peak around 62° corresponds to graphite (103) planes, which is seen in other ball-milled graphite samples as well.[35] The XRD spectrum confirms the presence of pure

CMTs devoid of gallium, with properties quite similar to those of ball-milled graphite.

The specific capacity retention of CMTs with Li ion intercalation is presented in Figure 3a. The initial discharge capacity is close to 1014 mAh g^{-1}, whereas the second discharge capacity is close to 826 mAh g^{-1} at a current density of 25 mA g^{-1}. The initial high capacity indicates a Li stoichiometry of $Li_{2.7}C_6$, which is similar to that observed for ball-milled SWCNTs.[7] The second cycle ratio drops to $Li_{2.3}C_6$. It is, however, interesting to see that there is also a steep drop in the third discharge cycle, and then, the specific capacity remains fairly constant with a value of 443 mAh g^{-1} after 20 cycles. The capacity retention after the third cycle is close to $Li_{1.6}C_6$ and remains fairly constant over the next 20 cycles, corresponding to 1.2 Li atoms per 6 carbon atoms ($Li_{1.2}C_6$). The specific capacity testing has been repeated with different mass loadings of the samples, and the results obtained correspond well to the capacity above. Specific capacity curves with a different mass loading has been presented in the Supporting Information (Figure S2). The capacity retention for the MWCNTs degrades to ~250 mAh g^{-1} after the first six cycles at a similar current density of 25 mA g^{-1} (Figure S3, Supporting Information). It can be clearly seen that the CMTs have a specific capacity that is at least 1.5 times that of the MWCNTs. The charge−discharge curves for the CMTs are also presented in Figure 3b, which show a steady charge and discharge capacity with cycling. Another interesting aspect of the present study is that the assembled cells were cycled between 3 V and 40 mV, 40 mV being higher than the usual low discharge voltages used for carbon-based materials. Even though going to lower voltages of around 10 mV can lead to significantly higher capacities, a higher potential cutoff will effectively prevent the Li from electroplating onto the material, which is a significant practical
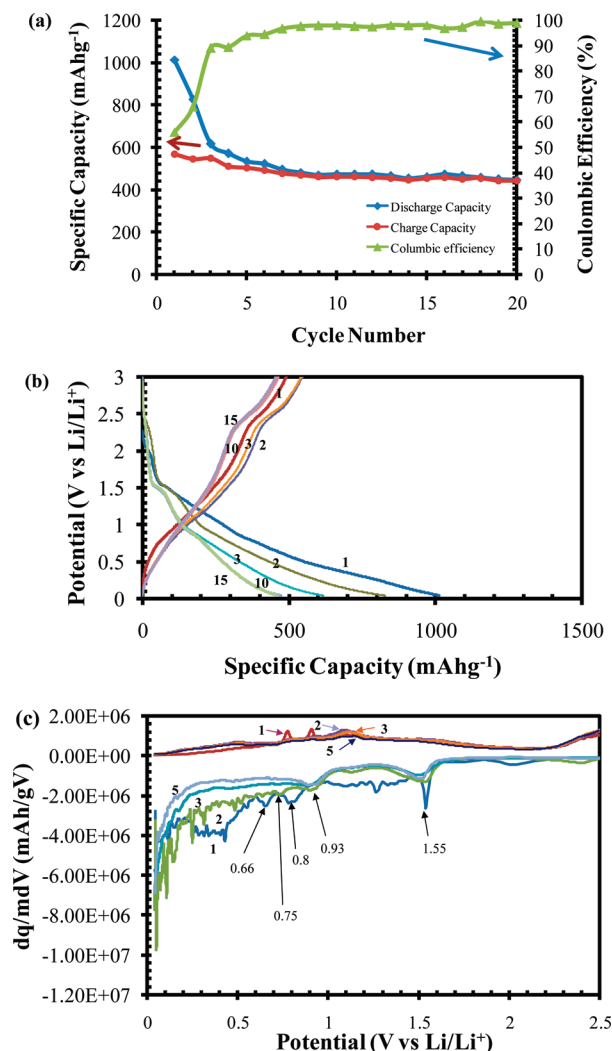
Figure 3. Electrochemical characteristics of CMTs. (a) Cyclic performance at a current density of 25 mAh g^{-1}. Coulombic efficiency is presented on the secondary axis to the right. (b) Charge−discharge curves indicating minimal capacity loss after three cycles. (c) Differential capacity curves of the first five cycles at a rate of 25 mAh g^{-1} between 3 V and 40 mV.

problem at high charge and discharge rates. The first cycle ratio $C_{rev}/(C_{rev} + C_{irrev})$ is close to 80%, which is higher than for most of the carbonaceous materials.[12,13,36] Similarly, the second cycle ratio is 75%, whereas the $C_{rev}/(C_{rev} + C_{irrev})$ ratio from the third cycle is over 93% and reaches 98% in the subsequent cycles, indicating a low irreversible capacity loss with cycling. The Coulombic efficiency is clearly plotted on the secondary axis of Figure 3a, showing 56% and 66% efficiencies for the first and the second cycles, respectively. The third cycle efficiency is 89% and, thereafter, remains above 97% up to 20 cycles. The average capacity loss "c" over a period of "n" number of cycles can be calculated as[12,13]
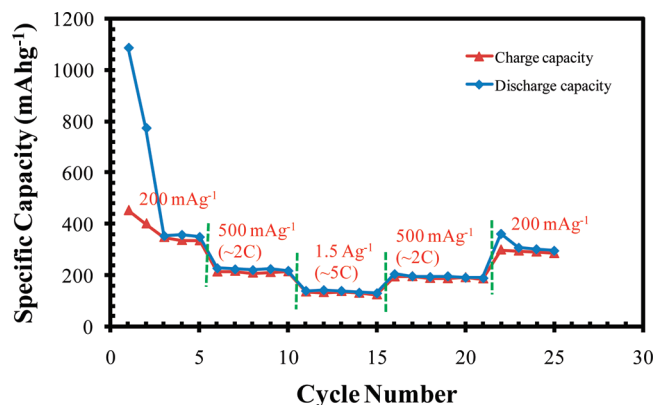
$$C_n \equiv C_1/(1 + cn) \qquad (2)$$

where C_n and C_1 are the specific capacities in the nth and first cycles, respectively. The average capacity loss in 20 cycles for the CMTs during the charge process is 1.3%, which is one of the lowest in carbon-based electrodes.[12,36] Similarly, the average capacity loss during the discharge process is

6.4%, in which the maximum capacity loss occurs during the first two cycles and then is quite low. The specific capacity curves shown in Figure 3b indicate a two-stage process of Li ion intercalation and deintercalation into the CMTs, starting at a discharge voltage of 1.5 V. The first stage is during low potentials of graphitized carbon, which is at potentials below 0.3−0.4 V. The second stage is the Li ion intercalation at potentials higher than 0.4 V all the way up to 1.5 V, evident in the specific capacity curves in Figure 3b and from the differential capacity curves shown in Figure 3c. The charge capacity retention between 1 and 2.3 V is close to 120 mAh g^{-1}, which can limit the application of CMTs as an ideal anode material. The charge capacity between 2.3 and 3 V is close to 100 mAh g^{-1}. High capacity retention in this region can be attributed to pseudocapacitance behavior that occurs due to the high attraction between the Li ions and the other charged species during Li intercalation, as a result of which the removal of the Li ions and the electrical double layer (Helmholtz layer) becomes less favorable.[37] The second stage intercalation that occurs at disordered graphite array stackings leads to turbostratic disorders, as shown later in the Raman spectroscopy and XRD analysis. The first discharge cycle differential capacity curve shows peaks at 0.66 and 0.8 V that correspond to the decomposition of the electrolyte and its reaction with the anode surface, forming the solid electrolyte interface (SEI). Evidently, there is a small peak during the second discharge cycle at 0.75 V, which indicates the further formation of the SEI layer. Further differential capacity curves until the fifth cycle do not indicate the presence of the peaks at 0.66 and 0.8 V, confirming the fact that the SEI is formed only during the first two cycles, which corresponds well with a significant drop in capacity during the first 2 discharge cycles, followed by a low capacity loss over the next 20 cycles. The first DC curve shows a redox peak at 1.55 V, and the second cycle shows two distinct peaks at 0.93 and 1.54 V. These peaks arise due to the Li ion diffusion and intercalation into the open ends and/or from the defect sites on the walls of the CMTs.[38-40] Moreover, these peaks also indicate shorter Li ion diffusion lengths and lower diffusion barriers inside the material. The Li ion diffusion time constant into a material can be deduced as $t = L^2/D$, where "L" is the Li ion diffusion length inside the material and "D" is the Li ion diffusion coefficient inside the material. D inside the carbonaceous materials decreases with either a decrease in the diffusion length or an increase in the diffusion coefficient. As the time constant decreases, the power capability of the material increases. Because of the nanodomains of graphite in the walls of the CMTs, Li ion diffusion lengths decrease considerably, thereby increasing the rate capability. Cyclic voltammetry curves presented in Figure 4 clearly indicate peaks at 1.3, 0.62, and 0.25 V. The peak at 1.3 V corresponds to decomposition of linear carbonate solvent, which, in this case, is DEC. Similarly, the peak at 0.62 V corresponds to the decomposition of EC, which is observed for about five cycles, corresponding well with the drop in the capacity for the first five cycles. The peak at 0.25 V corresponds to the Li ion intercalation into CMTs, which is also observed during the reverse process (deintercalation). The specific capacity retention of these materials at different current densities is shown in Figure 5. It can be seen that the CMTs retain a specific capacity of 135 mAh g^{-1} at a current density of 1.5 A g^{-1} (5C rate), and the good reversibility of capacity with changing rates indicate that CMTs have a robust structure

Thin-Walled CMTs as Anodes in Li-Ion Batteries

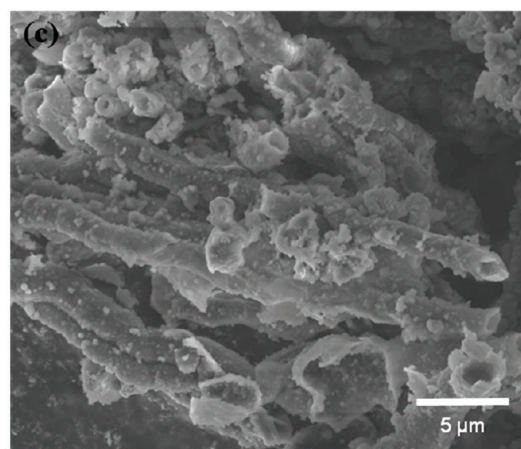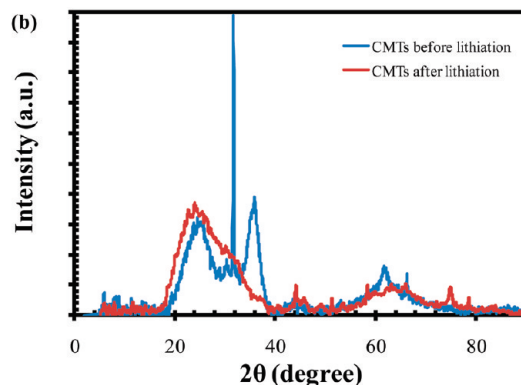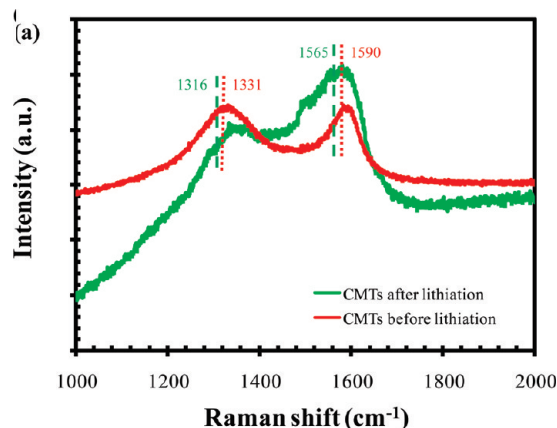*J. Phys. Chem. C, Vol. 114, No. 23, 2010* **10625**
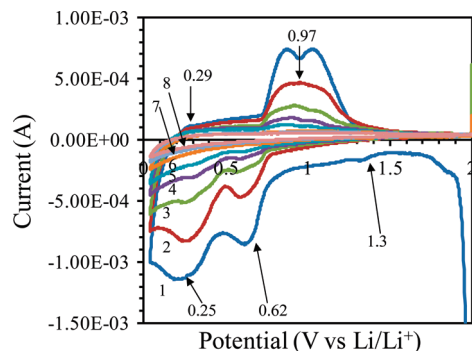
Figure 4. Cyclic voltammetry of CMTs indicating different peaks during the charge−discharge cycles for the first eight cycles.

**Figure 5.** CMTs' performance at different charge and discharge rates.

Figure 6. Post lithiation analysis of CMTs after 20 cycles. (a) Comparison of Raman spectra of pure and postlithiated CMTs. (b) The phase and structural changes in the material characterized by XRD. (c) SEM image showing the physical structure.

and show tremendous promise on improving the rate capabilities of carbon-based materials. The data presented in Table 1 indicate that the synthesis of CMTs in the present work is a lot faster than the other carbonaceous materials with a comparable rate performance, indicating a tremendous potential for large-scale synthesis. CMTs also exhibit good capacity retention for both low and high rates, unlike others presented in Table 1.

The postlithiated CMT samples have been characterized to better understand characteristics of Li ion intercalation and deintercalation. The Raman spectra for both the pure and the postlithiated CMTs are presented in Figure 6a. It can be seen that the G band shifts downward by 25 cm^{-1} after lithiation. The intercalation of the positive Li ions (donors in this case) changes the electron density of the graphite layers in which the charge is transferred to π bonds of graphite, resulting in the weakening of C−C intralayer bonds, leading to a downward shift of the G band in-plane stretching.[32] Similarly, the broadening of the D band as well as the blue shift by 20 cm^{-1} indicates that the graphene layers in the CMTs are further ruptured.[34] The additional peaks

between 1100 and 1400 cm^{-1} indicate that the energy states at these frequencies become active at finite material sizes, attributed to the random Li doping inside the material. The XRD analysis in Figure 6b indicates the disappearance of the other phases of graphite seen in the pure XRD spectra,

TABLE 1: Rate Performance of Carbon Microtubes Compared with the Other Carbonaceous Materials

	rate 1 [mA g^{-1}]	specific capacity [mAh g^{-1}]	rate 2 [A g^{-1}]	specific capacity [mAh g^{-1}]	large-area synthesis feasibility	reference
carbon microtubes	25	443 (20 cycles)	1.5	135 (5 cycles)	150 μm film (10 min)	present work
carbon nanofibers	~37	461 (2 cycles)	3.0	~170 (10 cycles)	>1 h	20
porous carbon monoliths	~75	<500 (40 cycles)	22.0	~70 (>10 cycles)	2 mm film (>6 days)	23
carbon nanosprings	50	~420 (3 cycles)	3.0	160 (>10 cycles)	>12 h	26
MWCNTs			3.0	47	commercially available	26
ball-milled CNTs	50	~595 after 1 cycle			>10 h	45
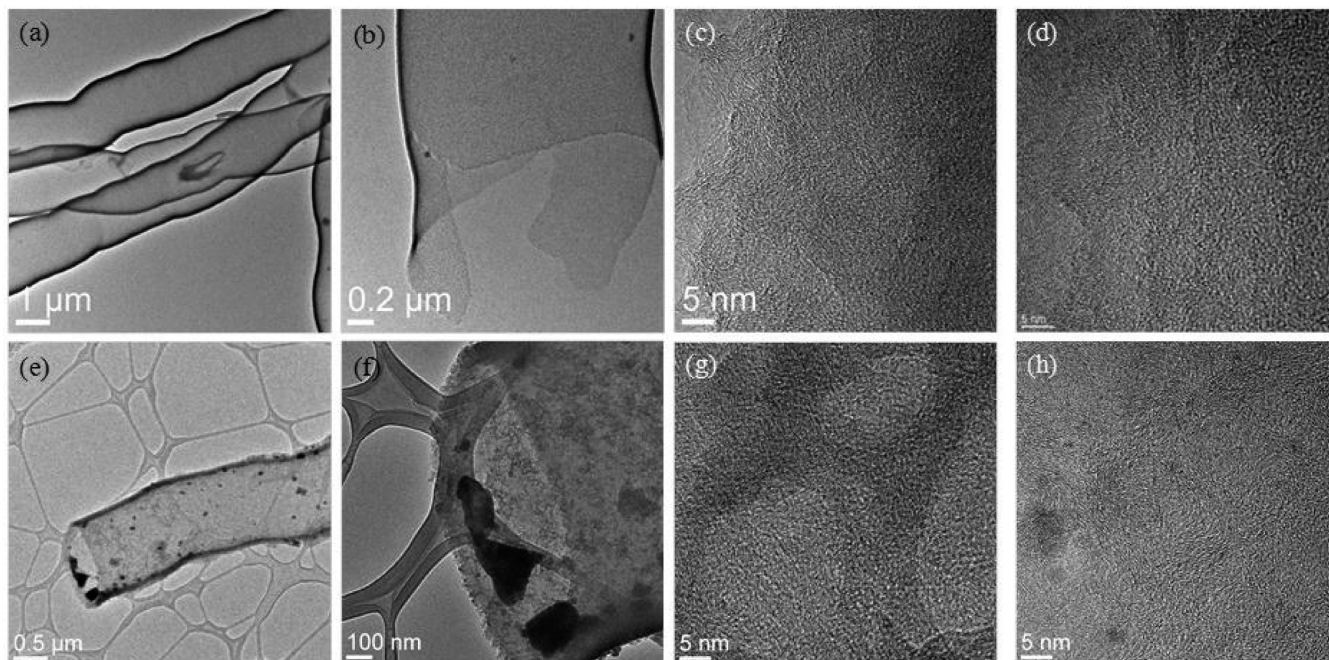
Figure 7. TEM images of CMTs. (a−d) Pure CMTs devoid of Ga after acid treatment prior to cycling measurements. (e−h) CMTs after 20 cycles of lithiation and delithiation showing the presence of the SEI layer, but the graphite nanodomains are still evident on the surface.

followed by the widening of the (002) peak of graphite. Such peak broadening is typical of intercalated carbon compounds.[41] Additionally, a small peak arises pertaining to the graphite (004) orientation. The stacking length of the CMTs, L_c, can be calculated using the (002) peak of the XRD spectra from the Scherrer formula[42]

$$L_c \equiv \frac{0.89\lambda}{B_c \cos\theta} \tag{3}$$

where λ is the X-ray wavelength and θ is the (002) Bragg peak. The crystallite size L_a of the graphite can be calculated using the intensity ratios of D and G bands of the Raman spectrum. It has been proven that the following Knight's relationship holds for graphite

$$L_a \equiv C\left(\frac{I_D}{I_G}\right)^{-1} \tag{4}$$

where $C = 8.3$ is a constant obtained from the Raman spectroscopy laser wavelength (632.8 nm)[43] and L_a has the units of nanometers. The intensity ratios in this case are the areas under the peak, unlike some of the other studies that compare the ratios of peak amplitude. In the case of pure CMTs, the stacking length is 1.92 nm with a lattice spacing of 3.53 Å, which accounts for about five to six stacking layers of graphite with an average crystallite size (L_a) of 7.9 nm. In the case of lithiated CMTs, it can be seen that the stacking length drops significantly to 0.76 nm with two layers of graphite while the crystallite size increased to 23.7 nm, which is explained by the fact that the CMT walls become more disorderly with Li ion intercalation and deintercalation. The SEM image in Figure 6c of the postlithiated sample indicates the stable physical tube structure of the CMTs even after 20 cycles but gives no information about the graphite nanodomain structures. Figure 7 shows the TEM images of

CMTs before and after lithiation. The high-resolution images show the presence of graphite nanodomains even after lithiation. The low-resolution image shows the presence of the SEI layer on the surfaces of thin walls of CMTs, but is not predominant. Nanographite domains of ∼8 nm exist within the thin walls of CMTs, which are close to ∼50 nm. Postlithiated images show graphite domains with an increased domain size consistent with the results obtained using the Raman and XRD analysis, but they still retain the crystallinity. Once the Li ions pass through the SEI layer on the surface, they are intercalated easily and completely into the available nanodomains, which explains the good capacity retention of CMTs. On the basis of all these results, a simple mechanism can be proposed for the Li ion intercalation into the CMTs.

The mechanism of Li intercalation and deintercalation can be explained as follows:

(i) The CMT walls have nanographite domains of graphite, which precisely have five to six graphene layers with an average crystallite size of 7.9 nm.

(ii) The Li ions enter the inside walls through the defect sites along with the diffusion from the tube ends into these nanographite domains.

(iii) Repeated Li ion cycling cracks the defect sites further, showing a significant drop in the stacking length of the nanodomains to about two graphene layers with an increase in the crystallite size, probably from the volume expansion of the crystallite on lithium intercalation. Overall, the disorder of the nanodomains increases as a result of the lithiation.

In principle, the Li ions follow the model proposed by Dahn and co-workers[5,6] which proposes that Li ions are adsorbed on both sides of the graphene sheets in disordered structures, in the defect structures composed of stacking faults[44] and in the internal interfaces, resulting in excessive storage of Li.

Conclusions

In summary, for the first time, CMTs have been synthesized on large-area substrates and tested as possible anode candidates

Thin-Walled CMTs as Anodes in Li-Ion Batteries

J. Phys. Chem. C, Vol. 114, No. 23, 2010 **10627**

for Li-ion batteries. CMTs have shown a capacity of 450 mAh g^{-1} after 20 cycles, ~1.5 times higher than MWCNTs. The average charge capacity loss is reported to be 1.3%, which is quite low for carbon-based materials. CMTs have also shown to be able to withstand high rates with a capacity retention of 135 mAh g^{-1} at a current density of 1.5 A g^{-1} and then reversibly achieve the original capacity at lower rates. It is inferred from the postlithiation analysis that the nanodomains of graphite in the walls of the CMTs and the open ends of CMTs provide various channels for Li intercalation. The Li ion diffusion lengths can significantly decrease because of this, resulting in an excellent performance of the CMTs over a wide range of charge−discharge rates.

Supporting Information Available: The EDAX spectrum indicating that the cleaned CMTs are devoid of Ga is presented. The specific capacity performance of CMTs using a different mass loading and of MWCNTs is also presented. This material is available free of charge via the Internet at http://pubs.acs.org.

References and Notes

(1) Scrosati, B. *Nature* **1995**, *373*, 557–558.

(2) Tarascon, J. M.; Armand, M. *Nature* **2001**, *414*, 359–367.

(3) Fong, R.; Vonsacken, U.; Dahn, J. R. *J. Electrochem. Soc.* **1990**, *137*, 2009–2013.

(4) Dahn, J. R.; Zheng, T.; Liu, Y. H.; Xue, J. S. *Science* **1995**, *270*, 590–593.

(5) Zheng, T.; Xing, W.; Dahn, J. R. *Carbon* **1996**, *34*, 1501–1507.

(6) Dahn, J. R.; Xing, W.; Gao, Y. *Carbon* **1997**, *35*, 825–831.

(7) Gao, B.; Kleinhammes, A.; Tang, X. P.; Bower, C.; Fleming, L.; Wu, Y.; Zhou, O. *Chem. Phys. Lett.* **1999**, *307*, 153–157.

(8) Wang, X. X.; Wang, J. N.; Chang, H.; Zhang, Y. F. *Adv. Funct. Mater.* **2007**, *17*, 3613–3618.

(9) Masarapu, C.; Subramanian, V.; Zhu, H.; Wei, B. *Adv. Funct. Mater.* **2009**, *19*, 1008–1014.

(10) Kim, C.; Yang, K. S.; Kojima, M.; Yoshida, K.; Kim, Y. J.; Kim, Y. A.; Endo, M. *Adv. Funct. Mater.* **2006**, *16*, 2393–2397.

(11) Lee, K. T.; Lytle, J. C.; Ergang, N. S.; Oh, S. M.; Stein, A. *Adv. Funct. Mater.* **2005**, *15*, 547–556.

(12) Zhou, H.; Zhu, S.; Hibino, M.; Honma, I.; Ichihara, M. *Adv. Mater.* **2003**, *15*, 2107–2111.

(13) Frakowiak, E.; Gautier, S.; Gaucher, H.; Bonnamy, S.; Beguin, F. *Carbon* **1999**, *37*, 61–69.

(14) Frakowiak, E.; Beguin, F. *Carbon* **2002**, *40*, 1775–1787.

(15) Adelhelm, P.; Hu, Y. S.; Antonietti, M.; Maier, J.; Smarsly, B. M. *J. Mater. Chem.* **2009**, *19*, 1616–1620.

(16) Poizot, P.; Laruelle, S.; Grugeon, S.; Dupont, L.; Tarascon, J. M. *Nature* **2000**, *407*, 496–499.

(17) Park, M. S.; Wang, G. X.; Kang, Y. M.; Wexler, D.; Dou, S. X.; Liu, H. K. *Angew. Chem., Int. Ed.* **2007**, *46*, 750–753.

(18) Meduri, P.; Pendyala, C.; Kumar, V.; Sumanasekera, G. U.; Sunkara, M. K. *Nano Lett.* **2009**, *9*, 612–616.

(19) Chan, C. K.; Peng, H. L.; Liu, G.; McIlwrath, K.; Zhang, X. F.; Huggins, R. A.; Cui, Y. *Nat. Nanotechnol.* **2008**, *3*, 31–35.

(20) Subramanian, V.; Zhu, H.; Wei, B. *J. Phys. Chem. B* **2006**, *110*, 7178–7183.

(21) Li, N.; Mitchell, D. T.; Lee, K. P.; Martin, C. R. *J. Electrochem. Soc.* **2003**, *150*, 979.

(22) Disma, F. S.; Lenain, C.; Beaudoin, B.; Aymard, L.; Tarascon, J. M. *Solid State Ionics* **1997**, *98*, 145.

(23) Hu, Y. S.; Adelhelm, P.; Smarsly, B. M.; Hore, S.; Antonietti, M.; Maier, J. *Adv. Funct. Mater.* **2007**, *17*, 1873–1878.

(24) Wang, H.; Abe, T.; Maruyama, S.; Iriyama, Y.; Ogumi, Z.; Yoshikawa, K. *Adv. Mater.* **2007**, *17*, 2857.

(25) Sano, A.; Kurihara, M.; Abe, T.; Ogumi, Z. *J. Electrochem. Soc.* **2009**, *156*, 682.

(26) Wu, X. L.; Liu, Q.; Guo, Y. G.; Song, W. G. *Electrochem. Commun.* **2009**, *11*, 1468–1471.

(27) Hu, J.; Bando, Y.; Xu, F.; Li, Y.; Ahan, J.; Xu, J. *Adv. Mater.* **2004**, *16*, 153–156.

(28) Bhimarasetti, G.; Sunkara, M. K.; Graham, U. M.; Davis, B. H.; Suh, C.; Rajan, K. *Adv. Mater.* **2003**, *15*, 1629–1632.

(29) Bhimarasetti, B.; Cowley, J. M.; Sunkara, M. K. *Nanotechnology* **2005**, *16*, S362–S369.

(30) Park, C.; Kim, J.; Yoon, D.; Han, S.; Doh, C.; Yeo, S.; Lee, K. H.; Anderson, T. J. *J. Electrochem. Soc.* **2005**, *152*, C298–C303.

(31) Yu, Y.; Gu, L.; Zhu, C.; van Aken, P. A.; Maier, J. *J. Am. Chem. Soc.* **2009**, *131*, 15984–15985.

(32) Wang, Z.; Huang, X.; Xue, R.; Chen, L. *Carbon* **1999**, *37*, 685–692.

(33) Nemanich, R. J.; Solin, S. A. *Phys. Rev. B* **1979**, *20*, 392–401.

(34) Dillon, R. O.; Woollam, J. A.; Katkanant, V. *Phys. Rev. B* **1984**, *29*, 3482–3489.

(35) Welham, N. J.; Williams, J. S. *Carbon* **1998**, *36*, 1309–1315.

(36) Zheng, T.; Mckinnon, W. R.; Dahn, J. R. *J. Electrochem. Soc.* **1996**, *143*, 2137–2145.

(37) Levi, M. D.; Aurbach, D. *Electrochim. Acta* **1999**, *45*, 167–185.

(38) Shimoda, H.; Gao, B.; Tang, X. P.; Kleinhammes, A.; Fleming, L.; Wu, Y.; Zhou, O. *Physica B* **2002**, *323*, 133–134.

(39) Shimoda, H.; Gao, B.; Tang, X. P.; Kleinhammes, A.; Fleming, L.; Wu, Y.; Zhou, O. *Phys. Rev. Lett.* **2002**, *88*, 015502.

(40) Disma, F.; Aymard, L.; Dupont, L.; Tarascon, J. M. *J. Electrochem. Soc.* **1996**, *143*, 3959–3972.

(41) Prasad, B. L. V.; Sato, H.; Enoki, T.; Hishiyama, Y.; Kaburagi, Y.; Rao, A. M.; Sumanasekera, G. U.; Eklund, P. C. *Phys. Rev. B* **2001**, *64*, 235407.

(42) Zheng, T.; Liu, Y.; Fuller, E. W.; Tseng, S.; Sacker, U. V.; Dahn, J. R. *J. Electrochem. Soc.* **1995**, *142*, 2581–2590.

(43) Matthews, M. J.; Pimenta, M. A.; Dresselhaus, G.; Dresselhaus, M. S.; Endo, M. *Phys. Rev. B* **1999**, *59*, R6585–R6588.

(44) Funabiki, A.; Inaba, M.; Ogumi, Z.; Yuasa, S.; Otsuji, J.; Tasaka, A. *J. Electrochem. Soc.* **1998**, *145*, 172–178.

(45) Gao, B.; Bower, C.; Lorentzen, J. D.; Fleming, L.; Kleinhammes, A.; Tang, X. P.; McNeil, L. E.; Wu, Y.; Zhou, O. *Chem. Phys. Lett.* **2000**, *327*, 69–75.